The dynamics of Ca^{2+} puffs: a study of instantaneously-coupled intracellular Ca^{2+} channels

A thesis submitted in partial fulfillment for the
degree of Bachelor of Science in Physics
at the College of William and Mary in Williamsburg, Virginia

Author: Vien Nguyen

Advisor: Dr. Greg D. Smith
Department of Applied Science

Abstract

In this paper we explore how different IP_3R Ca^{2+} channel models, from a simple two-state channel to much more complicated IP_3R models, synchronously gate when coupled. While most of the relevant prior work in this area has focused on single-channel kinetics of Ca^{2+}-regulated Ca^{2+} channels, we explore the effect of coupling such single channel models under the assumption of fast domain formation and collapse (i.e., instantaneous coupling) on the open probability of Ca^{2+} release sites as a collective entity. We show how the transition matrix for a Ca^{2+} release site can be constructed from the transition matrix of a single channel model of interest and we use Monte-Carlo simulation methods to perform several relevant parameter studies. With the minimal two-state and four-state channel models, we find that coupled Ca^{2+} channels can lead to so-called "puffing" behavior as indicated by a response measure we introduce: the puff *Score*. For several IP_3R channel models presented in the literature, we do not see robust puffs when these channels are instantaneously coupled. The effect of the spatial distribution of channels at Ca^{2+} release sites is also explored.

Contents

1 Introduction

During my first year working in the Smith laboratory (Fall 2001), I explored simple models of Ca^{2+}-channels, such as a two-state model presented below that includes Ca^{2+}-activation and a four-state model that includes both Ca^{2+}-activation and Ca^{2+}-inactivation (Sec. 3.1 and 3.2). Using ordinary differential equations and a diagrammatic method, I solved for the equilibrium open probability of both models and plotted each as a function of the background $[Ca^{2+}]$ (these were preliminary results leading to Figure 1). The next stage of my research involved deriving a representation of the infinitesimal generator matrix, or Q-matrix, for these single channel models. This was preliminary to my real objective, which was to see how instantaneously-coupled two-state and four-state channels collectively gated. This required expanding the Q-matrix for a single channel to describe states and transition rates for multiple channels with the assumption of instantaneous coupling via a Ca^{2+} microdomain that forms and collapses on a time-scale much faster than the channel kinetics. (Sec. 3.4 and 3.6). With the help of Dr. Smith, I discovered that the form of these expanded Q-matrices could be written compactly using Kronecker products and Kronecker sums.

Nevertheless, it became apparent that as we increased the number of channels in our cluster, the matrix size would expand exponentially, and after about 10 or so channels it became too large for computational simulations. At this point I am indebted to Drs. Smith and Mathias for the development of a numerical approach (not discussed here) for solving the stationary probability distribution of release sites containing 7 or 19 channels. Using MATLAB codes developed by Dr. Smith, I was able to model 20 channels easily.

My next task was to run simulations to see whether or not any of the models would show puffing behavior. To our surprise, parameters could be found for both models that lead to robust puffing behavior (i.e., synchronous gating). More discussions followed and we now believe the puffs generated by these two models are terminated by two fundamentally different mechanisms (Ca^{2+} inactivation versus stochastic attrition).

At this point, Dr. Smith and I wrote a manuscript detailing our work, which was submitted to the *Bulletin of Mathematical Biology* on January 6, 2004 [1]. The paper was

revised and resubmitted on July 15, 2004, and has been available online since November 26, 2004. After the manuscript was published, my research focused on working with more realistic IP_3R models found in the literature, and applying the same techniques to see whether these more realistic IP_3R models exhibited Ca^{2+} puffs.

The remainder of the manuscript is organized as follows. First, I describe how Ca^{2+}-regulated Ca^{2+} release sites can be derived from single-channel models with Ca^{2+} activation (IP_3R-2), Ca^{2+} inactivation, or both (IP_3R-1). Such models are *stochastic automata networks* (SANs) with a large number of so-called functional transitions [2,3]. Sections 3 to 4, as well as figures 1 through 8, come from the published manuscript mentioned above and are representative of the work that I performed in Dr. Smith's lab, though Dr. Smith extended my preliminary results when creating the final published versions. Sections 5 to 7 detail my continuing work this year, using more advanced, realistic IP_3R models such as the Fraiman-Ponce Dawson model [4]. Figures 10 to 14 in these sections are entirely my own construction. Finally, Section 8 explores the effect of different spatial arrangements on the range of puff *Scores*.

2 Background

Localized Ca^{2+} elevations known as Ca^{2+} 'puffs' and 'sparks' are cellular signals of great interest. Ca^{2+} puffs, sparks, and localized Ca^{2+} increases due to plasma membrane Ca^{2+} channels are not only the building blocks of global Ca^{2+} release events, but also highly specific regulators of cellular function [5–7].

Understanding the dynamics of Ca^{2+} puffs and sparks is complicated because of the clustering of intracellular Ca^{2+} channels, and the short range of action of intracellular Ca^{2+} [6,8]. For example, in the cortical regions of immature *Xenopus* oocytes (frog eggs), inositol 1,4,5-trisphosphate receptors (IP_3Rs) occur in clusters of 5–50 with inter-cluster spacing on the order of a few microns [9].

This spatial organization of intracellular Ca^{2+} channels is the basis of three distinct modes of Ca^{2+} mobilization observed in *Xenopus* oocytes via confocal microfluorimetry: 1) localized Ca^{2+} elevations from single channels (called Ca^{2+} blips), 2) Ca^{2+} elevations

due to the activation of multiple channels grouped within a single Ca^{2+} release site (called Ca^{2+} puffs) [10, 11], and 3) global responses such as oscillations and waves that involve multiple release sites. These three modes of Ca^{2+} release have been named fundamental, elementary, and global responses, respectively [6].

Similarly, the Ca^{2+} sparks observed in cardiac myocytes [12, 13] are elementary Ca^{2+} release events due to the concerted action of a cluster of ryanodine receptors (RyRs) while the fundamental Ca^{2+} release event, the Ca^{2+} quark, is a localized Ca^{2+} elevation due to the opening of a single channel [14]. In striated muscle, intracellular Ca^{2+} release via RyRs is tightly controlled by the membrane voltage sensor [15]. The phenomenon of Ca^{2+}-induced Ca^{2+} release in cardiac excitation-contraction coupling represents the coalescence of Ca^{2+} sparks, each triggered by plasma membrane Ca^{2+} channel activation and subsequent Ca^{2+} influx into a restricted sub-sarcolemmal compartment [12, 16].

The IP_3R exists in multiple isoforms and splice variants, three of which have been cloned [17]. The IP_3R isoforms have different sensitivities to IP_3 and are differentially regulated by Ca^{2+} [18]. Recent findings suggest that the 'bell-shaped' curve relating $[Ca^{2+}]$ to IP_3R open probability may not apply to all IP_3R isoforms [19–21]. In addition to being more active than the type 1 IP_3R at low $[Ca^{2+}]$, the type 3 IP_3R may [22] or may not [19] inactivate at high $[Ca^{2+}]$. The bell-shaped open probability curve of the type 1 IP_3R is transformed by high $[IP_3]$ [23]. While a myriad of IP_3R models reproduce aspects of IP_3R gating, many focus on the type 1 IP_3R [23–29] and include fast Ca^{2+}-activation, slower Ca^{2+}-inactivation, and regulation of the IP_3R by the co-agonist IP_3 (but see [30]).

Although there is consensus that Ca^{2+} puffs and sparks arise from the cooperative activity of clusters of IP_3Rs and RyRs, biophysical theory relating single-channel kinetics and the collective phenomena of stochastic Ca^{2+} excitability is not as well-developed as our understanding of the association of Ca^{2+} with endogenous and exogenous Ca^{2+} buffers (Ca^{2+}-binding proteins, chelators, and indicators) [8, 31–38]. The phenomena of Ca^{2+} activation and inactivation, co-agonist properties of IP_3Rs, and the dynamics of the buffered diffusion of intracellular Ca^{2+} presumably determine the amplitude, duration, and inter-event intervals of Ca^{2+} puffs [11, 39, 40].

3 Formulation of model

3.1 A two-state channel model with Ca^{2+} activation

Stochastic models of single channel gating often take the form of continuous-time discrete-state Markov processes (for review see [41,42]). For a two-state channel activated by Ca^{2+} the transition-state diagram is

$$\begin{array}{cccc} & & k^+c_\infty^\eta & \\ \text{(closed)} & C & \rightleftharpoons & O \quad \text{(open)} \\ & & k^- & \end{array} \tag{1}$$

where $k^+c_\infty^\eta$ and k^- are transition rates with units of reciprocal time, k^+ is an association rate constant with units of $\text{conc}^{-\eta}\,\text{time}^{-1}$, η is the cooperativity of Ca^{2+} binding, and c_∞ is the background $[Ca^{2+}]$. This transition state diagram corresponds to a discrete-state continuous-time Markov process, $X(t)$, that takes on values in the state-space $\mathcal{M} = (0,1) = (C,O)$. This well-known telegraph process is defined by the infinitesimal generator or Q-matrix,

$$Q = (q_{ij}) = \begin{pmatrix} -k^+c_\infty^\eta & k^+c_\infty^\eta \\ k^- & -k^- \end{pmatrix} \tag{2}$$

where the off-diagonal elements are given by

$$q_{ij} = \lim_{\Delta t \to 0} \frac{\mathsf{P}\{X(t+\Delta t) = \mathcal{M}_j | X(t) = \mathcal{M}_i\}}{\Delta t} \qquad (i \neq j)$$

and the diagonal elements are such that each row sum is zero, $\sum_j q_{ij} = 0$.

We write the stationary (time-independent) probability of being in state $\mathcal{M}_i$ as π_i or $\pi_{\mathcal{M}_i}$ and the stationary probability distribution as the row vector $\boldsymbol{\pi} = (\pi_0, \pi_1) = (\pi_C, \pi_O)$. The stationary distribution satisfies both conservation of probability ($\sum_i \pi_i = 1$) and global balance, that is, the probability flux into and out of each state is equal,

$$\sum_{i \neq j} \pi_i q_{ij} = \pi_j \sum_{i \neq j} q_{ji}. \tag{3}$$

These conditions can be written compactly as

$$\boldsymbol{\pi} Q = \mathbf{0} \qquad \text{subject to} \qquad \boldsymbol{\pi}\mathbf{e} = 1 \tag{4}$$

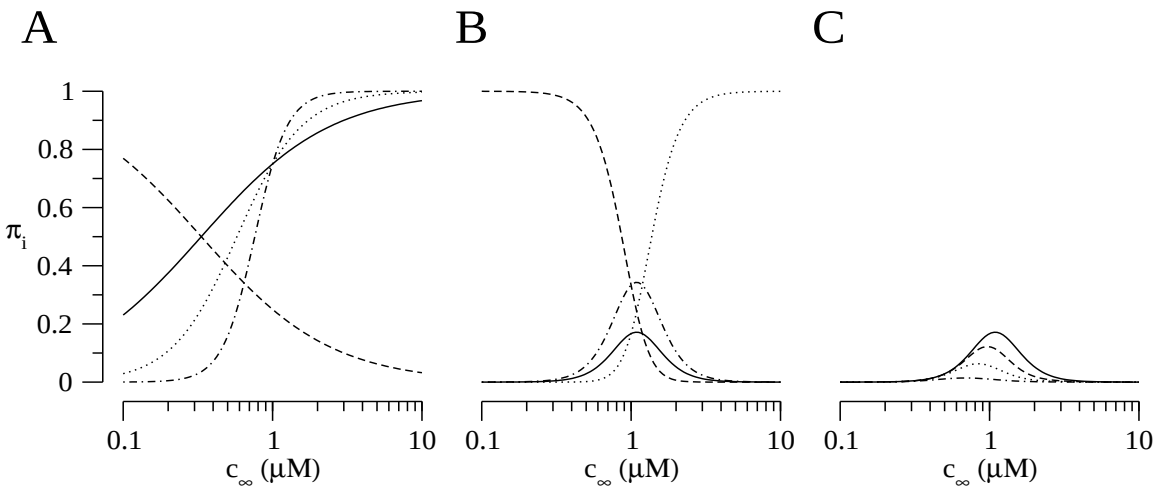

Figure 1: **A**: The steady-state probabilities for the closed π_C (*dashed line*) and open π_O (*solid line*) states of the two-state model as a function of the background $[Ca^{2+}]$ (c_∞) given by Eq. 5 with $k^+ = 1.5\ \mu M^{-2}\,ms^{-1}$, $k^- = 0.5\ ms^{-1}$, and $\eta = 1$. The *dotted* and *dot-dashed lines* show π_O for higher cooperativity ($\eta = 2$ and 4). **B**: The steady-state probabilities for the four-state model given by Eq. 14 assuming no domain Ca^{2+}-mediated inactivation. π_{C_1}, *dashed line*; π_O, *solid*; π_{C_2}, *dotted*; π_{C_3}, *dot-dashed*. Parameters in $\mu M^{-2}\,ms^{-1}$: $k_a^+ = 0.5$, $k_b^+ = 0.001$, $k_c^+ = 0.5$, $k_d^+ = 0.01$; in ms^{-1}: $k_a^- = 1$, $k_b^- = 0.001$, $k_c^- = 1$; k_d^- given by Eq. 7; $c_d = 0$. **C**: The four-state model π_O decreases as the domain $[Ca^{2+}]$ is increased. Parameters as **B** with $c_d = 0$, *solid line*; 1, *dashed*; 2, *dotted*; 4 μM, *dot-dashed*.

where **e** is a commensurate column vector of ones. Thus, for a two-state channel activated by Ca^{2+}, $\pi_C + \pi_O = 1$ and

$$\pi_C = \frac{k^-}{k^+ c_\infty^\eta + k^-} = \frac{K^\eta}{c_\infty^\eta + K^\eta} \qquad \pi_O = \frac{k^+ c_\infty^\eta}{k^+ c_\infty^\eta + k^-} = \frac{c_\infty^\eta}{c_\infty^\eta + K^\eta} \tag{5}$$

where K, the dissociation constant for the Ca^{2+} regulatory site, is given by $K^\eta = k^-/k^+$. As shown in Fig. 1A, the open probability (π_O) of the two-state channel increases as the background $[Ca^{2+}]$ increases and $c_\infty = K$ is the $[Ca^{2+}]$ leading to $\pi_O = 1/2$. Higher values of the cooperativity (η) lead to a steeper activation curves.

3.2 A four-state channel model with Ca^{2+} activation and inactivation

A transition state diagram for a four-state channel with both Ca^{2+}-inactivation (vertical) and Ca^{2+}-activation (horizontal) is

$$\begin{array}{ccccc} & & k_a^+ c_\infty^\eta & & \\ \text{(closed)} \quad C_1 & & \rightleftharpoons & & O \quad \text{(open)} \\ & & k_a^- & & \\ k_d^+ c_\infty^\eta \;\downarrow\uparrow\; k_d^- & & & & k_b^- \;\uparrow\downarrow\; k_b^+ (c_\infty + c_d)^\eta \\ & & k_c^- & & \\ \text{(closed)} \quad C_3 & & \leftrightharpoons & & C_2 \quad \text{(closed)} \\ & & k_c^+ c_\infty^\eta & & \end{array} \tag{6}$$

For simplicity we assume the cooperativities of Ca^{2+} binding (η) are the same and include transitions between the two inactivated states. Inactivation and de-inactivation are slow compared to activation and de-activation ($k_b^\pm, k_d^\pm << k_a^\pm, k_c^\pm$). Because this model includes a cycle we choose parameters that satisfy the thermodynamic constraint [43],

$$K_c K_d = K_a K_b,$$

where $K_i^\eta = k_i^-/k_i^+$ for $i \in \{a, b, c, d\}$ are dissociation constants. That is, there are eight rate constants in Eq. 6, but only seven are free parameters because

$$k_d^- = k_d^+ \frac{K_a K_b}{K_c}. \tag{7}$$

Enumerating states $\mathcal{M} = (0, 1, 2, 3) = (C_1, O, C_2, C_3)$, the infinitesimal generator corresponding to Eq. 6 is

$$Q = \begin{pmatrix} -k_a^+ c_\infty^\eta - k_d^+ c_\infty^\eta & k_a^+ c_\infty^\eta & 0 & k_d^+ c_\infty^\eta \\ k_a^- & -k_a^- - k_b^+ (c_\infty + c_d)^\eta & k_b^+ (c_\infty + c_d)^\eta & 0 \\ 0 & k_b^- & -k_b^- - k_c^- & k_c^- \\ k_d^- & 0 & k_c^+ c_\infty^\eta & -k_d^- - k_c^+ c_\infty^\eta \end{pmatrix}. \tag{8}$$

Notice that the four-state model has a complication in that one of the Ca^{2+}-mediated transitions ($O \to C_2$) occurs when the channel is open [44]. If the channel is conducting

Ca^{2+}, then the $[Ca^{2+}]$ experienced by the Ca^{2+} binding site will be significantly higher than c_∞. We indicate this by writing $c_\infty + c_d$ as the $[Ca^{2+}]$ determining the rate of the $O \to C_2$ transition, where c_d is 'domain Ca^{2+},' the increase in $[Ca^{2+}]$ above background experienced when the channel is open [26, 45].

Beginning with Eq. 4, the steady-state probability distribution of the four-state model is found to be

$$\pi_{C_1} = z_{C_1}/D \qquad \pi_O = z_O/D \qquad \pi_{C_2} = z_{C_2}/D \qquad \pi_{C_3} = z_{C_3}/D \tag{9}$$

where $D = z_{C_1} + z_O + z_{C_2} + z_{C_3}$ and

$$z_{C_1} = \kappa_b^+\kappa_c^-\kappa_d^- + \kappa_a^-\kappa_d^-\kappa_c^- + \kappa_b^-\kappa_a^-\kappa_d^- + \kappa_c^+\kappa_b^-\kappa_a^- \tag{10}$$

$$z_O = \kappa_d^+\kappa_c^+\kappa_b^- + \kappa_c^-\kappa_d^-\kappa_a^+ + \kappa_d^-\kappa_a^+\kappa_b^- + \kappa_a^+\kappa_b^-\kappa_c^+ \tag{11}$$

$$z_{C_2} = \kappa_b^+\kappa_d^+\kappa_c^+ + \kappa_a^-\kappa_d^+\kappa_c^+ + \kappa_d^-\kappa_a^+\kappa_b^+ + \kappa_a^+\kappa_b^+\kappa_c^+ \tag{12}$$

$$z_{C_3} = \kappa_d^+\kappa_b^+\kappa_c^- + \kappa_a^-\kappa_d^+\kappa_c^- + \kappa_b^-\kappa_a^-\kappa_d^+ + \kappa_a^+\kappa_b^+\kappa_c^- \tag{13}$$

where $\kappa_i^- = k_i^-$ for $i \in \{a, b, c, d\}$, $\kappa_i^+ = k_i^+ c_\infty^\eta$ for $i \in \{a, c, d\}$, and $\kappa_b^+ = k_b^+ (c_\infty + c_d)^\eta$. When the channel is not conducting Ca^{2+} ($c_d = 0$), these expressions reduce considerably,

$$\pi_{C_1} = K_b K_a / D_0 \qquad \pi_O = K_b c_\infty^\eta / D_0 \qquad \pi_{C_2} = c_\infty^{2\eta} / D_0 \qquad \pi_{C_3} = K_c c_\infty^\eta / D_0 \tag{14}$$

where the $K_i^\eta = k_i^-/k_i^+$ and $D_0 = K_b K_a + K_b c_\infty^\eta + c_\infty^{2\eta} + K_c c_\infty^\eta$.

Figure 1B shows the steady-state open probability of the four-state model as a function of the background $[Ca^{2+}]$ (c_∞). Because the four-state model includes Ca^{2+} inactivation, $\pi_O \to 0$ as $c_\infty \to \infty$. Conversely, in the two-state model that lacks Ca^{2+} inactivation, $\pi_O \to 1$ as $c_\infty \to \infty$ (Fig. 1A). Fig. 1C shows the open probability of the four-state model is dependent on domain $[Ca^{2+}]$—increasing c_d leads to decreased π_O for any value of c_∞.

3.3 The general form of single channel models

If we define the $M \times 1$ column vector $\mathbf{u}$ to indicate open states, both the two-state and four-state models can be written compactly as

$$Q = K_- + \mathrm{diag}\left(c_\infty \mathbf{e} + c_d \mathbf{u}\right)^\eta K_+ \tag{15}$$

where the matrices K_- and K_+ involve the dissociation and association rate constants, respectively. For the two-state channel $\mathbf{u} = (0,1)^T$ and

$$Q = \begin{pmatrix} 0 & 0 \\ k^- & -k^- \end{pmatrix} + \begin{pmatrix} c_\infty & 0 \\ 0 & c_\infty + c_d \end{pmatrix}^\eta \begin{pmatrix} -k^+ & k^+ \\ 0 & 0 \end{pmatrix},$$

though c_d doesn't survive the matrix multiplication. In the case of the four state model, $\mathbf{u} = (0,1,0,0)^T$ and

$$Q = \begin{pmatrix} \diamond & & & \\ k_a^- & \diamond & & \\ & k_b^- & \diamond & k_c^- \\ k_d^- & & & \diamond \end{pmatrix} + \begin{pmatrix} c_\infty & & & \\ & c_\infty + c_d & & \\ & & c_\infty & \\ & & & c_\infty \end{pmatrix}^\eta \begin{pmatrix} \diamond & k_a^+ & & k_d^+ \\ & \diamond & k_b^+ & \\ & & \diamond & \\ & & k_c^+ & \diamond \end{pmatrix}$$

where here and below a diamond ($\diamond$) indicates a diagonal element leading to a zero row sum in Q. Eq. 15 represents the general form of a single channel model with both background and domain Ca^{2+}-mediated transitions.

3.4 *Q*-matrix expansion for independent channels

If we write $Q^{(1)}$ for the $M \times M$ generator matrix of a single channel model such as Eq. 2 or Eq. 8, then the generator matrix $Q^{(2)}$ for two identical and independent channels is $M^2 \times M^2$ and given by,

$$Q^{(2)} = Q^{(1)} \oplus Q^{(1)} = Q^{(1)} \otimes I^{(1)} + I^{(1)} \otimes Q^{(1)}$$

where $\otimes$ and $\oplus$ are respectively the Kronecker product and sum [46, 47] and $I^{(1)}$ is the $M \times M$ identity matrix with the superscript indicating it has the size of $Q^{(1)}$. That is, the generator matrix for two independent two-state channels is

$$Q^{(2)} = \left(\begin{array}{cc|cc} \diamond & k^+ c_\infty^\eta & k^+ c_\infty^\eta & 0 \\ k^- & \diamond & 0 & k^+ c_\infty^\eta \\ \hline k^- & 0 & \diamond & k^+ c_\infty^\eta \\ 0 & k^- & k^- & \diamond \end{array}\right)$$

where the expanded state space is ordered lexicographically, $\mathcal{M}^{(2)} = (0, \cdots, 3) = (CC, CO, OC, OO)$, that is, as a binary representation of the indices with open states ones and closed states

zeros. Although the channels are identical, it is helpful to think of the left digit in each release site configuration as representing the state of the channel just introduced (channel 2).

The addition of a third independent channel gives

$$\begin{aligned} Q^{(3)} = Q^{(1)} \oplus Q^{(2)} &= Q^{(1)} \otimes I^{(1)} \otimes I^{(1)} + I^{(1)} \otimes Q^{(1)} \otimes I^{(1)} + I^{(1)} \otimes I^{(1)} \otimes Q^{(1)} \\ &= Q^{(1)} \otimes I^{(2)} + I^{(1)} \otimes Q^{(1)} \otimes I^{(1)} + I^{(2)} \otimes Q^{(1)} \end{aligned}$$

that is,

$$Q^{(3)} = \left(\begin{array}{cccc|cccc} \diamond & k^+c_\infty^\eta & k^+c_\infty^\eta & & k^+c_\infty^\eta & & & \\ k^- & \diamond & & k^+c_\infty^\eta & & k^+c_\infty^\eta & & \\ k^- & & \diamond & k^+c_\infty^\eta & & & k^+c_\infty^\eta & \\ & k^- & k^- & \diamond & & & & k^+c_\infty^\eta \\ \hline k^- & & & & \diamond & k^+c_\infty^\eta & k^+c_\infty^\eta & \\ & k^- & & & k^- & \diamond & & k^+c_\infty^\eta \\ & & k^- & & k^- & & \diamond & k^+c_\infty^\eta \\ & & & k^- & & k^- & k^- & \diamond \end{array}\right)$$

where

$$\mathcal{M}^{(3)} = (0, \cdots, 7) = (CCC, CCO, COC, COO, OCC, OCO, OOC, OOO)\,. \tag{16}$$

We can continue this process to any desired number of channels, say N, accounting for each additional independent channel with the recursive formula

$$Q^{(n+1)} = Q^{(1)} \oplus Q^{(n)} = Q^{(1)} \otimes I^{(n)} + I^{(1)} \otimes Q^{(n)} \tag{17}$$

eventually leading to the expanded generator matrix $Q^{(N)}$. Alternatively, we write $\oplus_{n=1}^{N}$ to indicate $N-1$ Kronecker sums and express the $M^N \times M^N$ matrix $Q^{(N)}$ compactly as

$$Q^{(N)} = \bigoplus_{n=1}^{N} Q^{(1)} = \sum_{n=1}^{N} I^{(N-n)} \otimes Q^{(1)} \otimes I^{(n-1)} \tag{18}$$

where $I^{(n)}$ is the identity matrix of size M^n.

In the language of computational probability, the expanded generator matrix $Q^{(N)}$ defined by Eq. 18 is a stochastic automata network (SAN) descriptor [48] for a collection

of identical and independently gating ion channels. This SAN descriptor takes a simple form precisely because the channels are assumed to gate independently. It can be shown with Kronecker product identities [49] that if $\boldsymbol{\pi}^{(1)}$ is the stationary distribution for the elementary generator matrix satisfying $\boldsymbol{\pi}^{(1)}Q^{(1)} = 0$ subject to $\boldsymbol{\pi}^{(1)}\mathbf{e}^{(1)} = 0$, then $\boldsymbol{\pi}^{(N)} = \bigotimes_{n=1}^{N} \boldsymbol{\pi}^{(1)} = \boldsymbol{\pi}^{(1)} \otimes \cdots \otimes \boldsymbol{\pi}^{(1)}$ solves $\boldsymbol{\pi}^{(N)}Q^{(N)} = 0$ subject to $\boldsymbol{\pi}^{(N)}\mathbf{e}^{(N)} = 1$. As might be expected the elements of the stationary distribution $\boldsymbol{\pi}^{(N)}$ take values consistent with a binomial or multinomial distribution with parameters N and $\pi_i^{(1)}$.

3.5 Geometry of problem and the steady-state Ca^{2+} microdomain

The interaction between channels in the Ca^{2+} release site model is mediated through the buffered diffusion of intracellular Ca^{2+}. Each channel participates in the Ca^{2+} microdomain and influences the local $[Ca^{2+}]$ experienced by other channels. For simplicity we assume the formation and collapse of the microdomain is fast compared to channel gating and the validity of superposing local $[Ca^{2+}]$ increases [36, 38]. Thus, channel interactions can be summarized by a $N \times N$ 'coupling matrix' $C = (c_{ij})$ that gives the increase (over c_∞) in $[Ca^{2+}]$ experienced by channel j when channel i is open. The diagonal elements of C represent domain Ca^{2+} (c_d).

To specify C we assume channels are localized on a planar ER membrane ($z = 0$). If we write $\mathbf{r}_i = x_i\hat{x} + y_i\hat{y}$ as the position of the pore of channel i, then assuming one high concentration Ca^{2+} buffer, the increase in $[Ca^{2+}]$ above background at $\mathbf{r} = x\hat{x} + y\hat{y} + z\hat{z}$ given by the excess buffer approximation is

$$c(\mathbf{r}) = \sum_i \frac{\sigma_i}{2\pi D|\mathbf{r}_i - \mathbf{r}|} e^{-|\mathbf{r}_i - \mathbf{r}|/\lambda} \tag{19}$$

where σ_i is the source amplitude of channel i in μmoles/sec and λ is the buffer space constant [31, 38]. If we assume identical source amplitudes,

$$\sigma_i(t) = \begin{cases} 0 & \text{channel } i \text{ closed} \\ \sigma_O & \text{channel } i \text{ open,} \end{cases}$$

and write $\mathbf{a}_j$ as the position of the Ca^{2+} regulatory site for channel j, the increase in

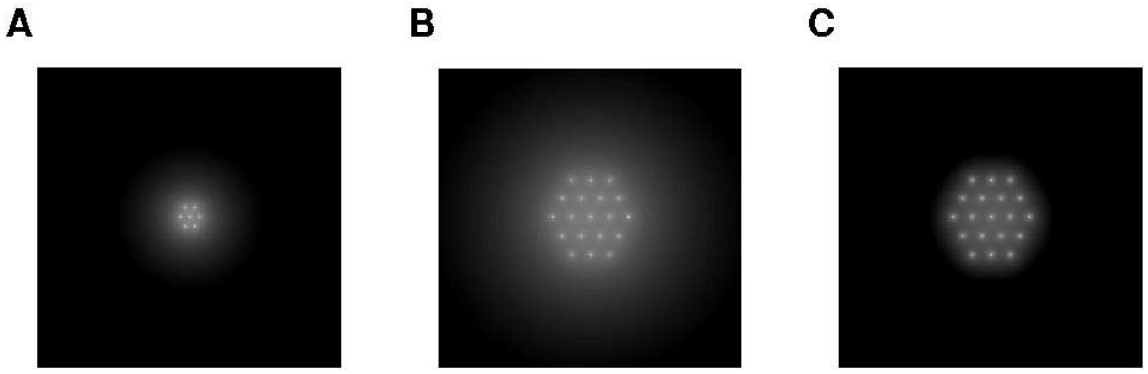

Figure 2: The excess buffer approximation (Eq. 19) gives the local $[Ca^{2+}]$, $c\,(x, y, z = 0)$, near 4×4 μm of planar ER membrane ($z = 0$). Intracellular Ca^{2+} channels are modeled as 0.05 pA point sources arranged in a hexagonal lattice of specified radius (R). Parameters: $D = 250$ $\mu m^2/s$, $\tau = 100$ ms, $\lambda = 5$ μm. **A**: $N = 7$, $R = 0.125$ μm. **B**: $N = 19$, $R = 0.6$ μm. **C**: Same as **B** except λ is decreased 10X, or, alternatively, the channel separation is increased 10X. The gray scale ranges from 50 nM (c_∞, *black*) to 100 μM (*white*).

$[Ca^{2+}]$ experienced by channel j when channel i is open is

$$c_{ij} = \frac{\sigma_O}{2\pi D|\mathbf{r}_i - \mathbf{a}_j|} e^{-|\mathbf{r}_i - \mathbf{a}_j|/\lambda}.$$

Assuming the regulatory sites are located a small distance r_d above channel pores, we write $\mathbf{a}_j = x_i\hat{x} + y_i\hat{y} + r_d\hat{z}$ and $r_{ij} = |\mathbf{r}_i - \mathbf{a}_j|$ so that $r_{ii} = |\mathbf{r}_i - \mathbf{a}_i| = r_d$. Thus, the off-diagonal elements of the coupling matrix $C = (c_{ij})$ are

$$c_{ij} = \frac{\sigma_O}{2\pi D r_{ij}} e^{-r_{ij}/\lambda} \qquad (i \neq j)\,, \tag{20}$$

with identical diagonal elements given by

$$c_{ii} = c_d = \frac{\sigma_O}{2\pi r_d} e^{-r_d/\lambda}. \tag{21}$$

Notice that $r_{ij} = r_{ji}$ implies that the interaction matrix is symmetric ($c_{ij} = c_{ji}$).

Figures 2A and B show the Ca^{2+} microdomain given by Eq. 19 for release sites with 7 and 19 channels arranged in a hexagonal lattice. The buffer length constant (λ) and release site radius (R) determine the size of the Ca^{2+} microdomain and strength of channel interactions (compare Figs. 2B and C).

3.6 *Q*-matrix expansion for instantaneously-coupled two-state channels

Using the interaction matrix $C = (c_{ij})$ we extend the SAN descriptor for independent channels (Eq. 18) to channels instantaneously-coupled via the buffered diffusion of intracellular Ca^{2+}. For two interacting two-state channels C is 2×2 and the expanded Q-matrix is

$$Q^{(2)} = \begin{pmatrix} \diamond & k^+ c_\infty^\eta & k^+ c_\infty^\eta & \cdot \\ k^- & \diamond & \cdot & k^+ (c_\infty + c_{21})^\eta \\ k^- & \cdot & \diamond & k^+ (c_\infty + c_{12})^\eta \\ \cdot & k^- & k^- & \diamond \end{pmatrix}. \tag{22}$$

For three interacting channels C is 3×3 and

$$Q^{(3)} = \begin{pmatrix} \diamond & k^+ c_\infty^\eta & k^+ c_\infty^\eta & \cdot & k^+ c_\infty^\eta & \cdot & \cdot & \cdot \\ k^- & \diamond & \cdot & k^+ (c_\infty + c_{12})^\eta & \cdot & k^+ (c_\infty + c_{13})^\eta & \cdot & \cdot \\ k^- & \cdot & \diamond & k^+ (c_\infty + c_{21})^\eta & \cdot & \cdot & k^+ (c_\infty + c_{23})^\eta & \cdot \\ \cdot & k^- & k^- & \diamond & \cdot & \cdot & \cdot & k^+ (c_\infty + c_{13} + c_{23})^\eta \\ k^- & \cdot & \cdot & \cdot & \diamond & k^+ (c_\infty + c_{31})^\eta & k^+ (c_\infty + c_{32})^\eta & \cdot \\ \cdot & k^- & \cdot & \cdot & k^- & \diamond & \cdot & k^+ (c_\infty + c_{12} + c_{32})^\eta \\ \cdot & \cdot & k^- & \cdot & k^- & \cdot & \diamond & k^+ (c_\infty + c_{13} + c_{23})^\eta \\ \cdot & \cdot & \cdot & k^- & \cdot & k^- & k^- & \diamond \end{pmatrix}. \tag{23}$$

Notice how the Ca^{2+} microdomain complicates the expanded generator matrix. For example, the element $q_{48}^{(3)}$ represents the configuration change $COO \rightarrow OOO$ where channel 3 makes a $C \rightarrow O$ transition under the influence of local $[Ca^{2+}]$ contributed by channel 1 (c_{13}), channel 2 (c_{23}), and the background (c_∞). Because the two-state single channel model (Eq. 1) has no domain Ca^{2+}-mediated transitions, the diagonal elements of C ($c_{ii} = c_d$) do not appear in Eq. 22 or Eq. 23.

If we write the coupling matrix C as N columns, C_{*j}, where $1 \leq j \leq N$, the $[Ca^{2+}]$ relevant for a transition out of state (row) j are restricted to the column C_{*j}. If $U = (u_{ij}) = (\mathbf{u}_1, \mathbf{u}_2, \cdots, \mathbf{u}_N)$, is a $M^N \times N$ matrix indicating if channel j is open in release site configuration i, then the local $[Ca^{2+}]$ used in entry $q_{ij}^{(N)}$ is $c_\infty + U_{i*} C_{*j}$ where U_{i*} is a $1 \times N$ row vector indicating open channels for configuration i. Until storage

requirements become a concern, the expanded Q-matrix for interacting Ca^{2+} channels can be efficiently built by constructing the matrix U column-by-column using Kronecker products. Recalling that $\mathbf{u}^{(1)}$ indicates the opens state(s) in the single channel model, column j of U is

$$U_{*j} = \mathbf{e}^{(N-j)} \otimes \mathbf{u}^{(1)} \otimes \mathbf{e}^{(j-1)} \tag{24}$$

where $\mathbf{e}^{(n)}$ is a $M^n \times 1$ column vector of ones.

3.7 *Q*-matrix expansion for instantaneously-coupled channels — general case

We skip the Q-matrix expansion for interacting four-state channels and instead consider the general case. Beginning with an elementary Q matrix in the form of Eq. 15,

$$Q^{(1)} = K_-^{(1)} + \mathrm{diag}\left(c_\infty \mathbf{e}^{(1)} + c_d \mathbf{u}^{(1)}\right)^\eta K_+^{(1)}, \tag{25}$$

the expanded Q-matrix for N channels coupled through the interaction matrix C can be written

$$Q^{(N)} = Q_-^{(N)} + Q_+^{(N)} \tag{26}$$

where $Q_-^{(N)}$ is simply

$$Q_-^{(N)} = \bigoplus_{n=1}^{N} K_-^{(1)} = \sum_{n=1}^{N} I^{(N-n)} \otimes K_-^{(1)} \otimes I^{(n-1)}. \tag{27}$$

The entries of $Q^{(N)}$ involving local Ca^{2+}, $Q_+^{(N)}$, cannot be expressed using Kronecker sums as Eq. 27, but (after some thought) can be compactly written as

$$Q_+^{(N)} = \sum_{n=1}^{N} \mathrm{diag}\left(c_\infty \mathbf{e}^{(N)} + \Gamma_{*n}\right)^\eta \left(I^{(N-n)} \otimes K_+^{(1)} \otimes I^{(n-1)}\right)$$

where Γ_{*n} is the nth column of the $M^N \times N$ matrix Γ given by

$$\Gamma = UC. \tag{28}$$

The matrix $\Gamma = (\gamma_{ij})$ gives the increase in local $[Ca^{2+}]$ above c_∞ experienced by channel j when the release site is in configuration i.

With the compact representation of the generator matrix for a collection of instantaneously-coupled Ca^{2+} channels given by Eqs. 25–28, the formulation of the Ca^{2+} release site model is complete. In the terminology of computational probability, we have derived the SAN descriptor for N identical (but not independent) interacting single channel models (Eq. 25) by assuming the formation and collapse of the Ca^{2+} microdomain is fast compared to channel gating.

Section 3 focuses on the simulation and analysis of Ca^{2+} release site SAN descriptors (Eqs. 26–28) where the elementary matrices $Q^{(1)}$ and open state indicator $\mathbf{u}^{(1)}$ are given by the two-state (Eq. 2) or four-state (Eq. 8) models. Release site parameters include the number of channels, N; the single channel model used and associated rate constants (2 or 7, respectively); the cooperativity of Ca^{2+} binding, η; and the interaction matrix, C. For simplicity, we fix the rate constants of the single channel models, the hexagonal lattice arrangement of the release site (Fig. 2), the unitary current (σ_O), buffer equations (Eq. 19) and parameters (D, λ), and the domain [Ca^{2+}] (r_d and c_d), so that the coupling matrix C is specified through Eq. 20 and 21 by the release site radius (R).

4 Results for two- and four-state channel models

4.1 The Ca^{2+} release site model exhibits stochastic Ca^{2+} excitability

Figure 3 shows Ca^{2+} release site simulations using the expanded generator matrix given by Eqs. 26–28. Seven four-state channels arranged in a hexagonal lattice (Fig. 2A) lead to 4^7 configurations, but for simplicity we plot (N_{C_1}, N_O, N_{C_2}, N_{C_3}) as a function of time. The second row of Fig. 3 shows that for significant periods of time all channels are closed ($N_O = 0$), but occasionally a large number of channels open simultaneously (N_O approaches $N = 7$). This stochastic Ca^{2+} excitability is reminiscent of Ca^{2+} puffs.

Figure 4 shows robust stochastic Ca^{2+} excitability in a release sites composed of 19 four-state channels arranged as Fig. 2B, albeit with more 'blips' where one or more channels opens without activating the entire release site. Parameters are as Fig. 3 except

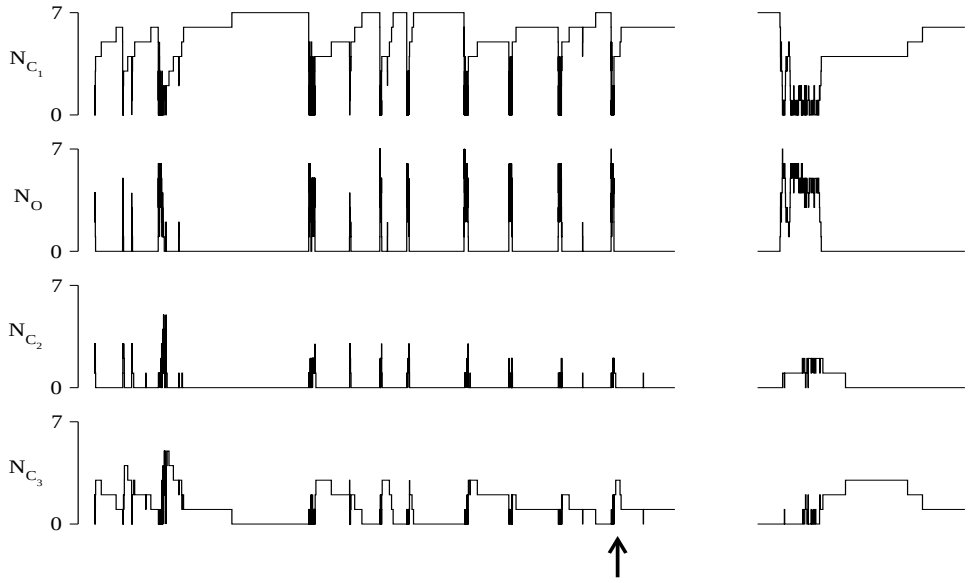

Figure 3: Ca^{2+} release site simulations with 7 four-state channels (Eq. 8) exhibit stochastic Ca^{2+} excitability reminiscent of Ca^{2+} puffs. Total time: 2 s (*left*) and 50 ms (*arrow*, *right*). For 5 trials the observed mean and variance of N_O are resp. 0.18 ± 0.04 and 0.80 ± 0.22 (mean ± SD) for a *Score* of 0.63. Parameters used: $R = 0.125$ μm, $r_d = 0.05$ μm, $\eta = 2$, $c_\infty = 50$ nM, and $k_i^\pm$ as Fig. 1B.

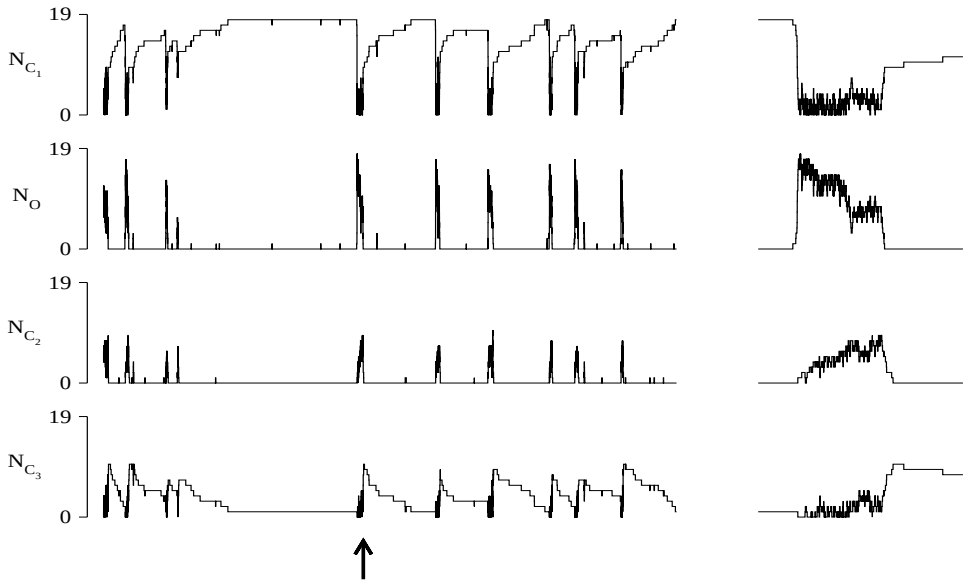

Figure 4: Ca^{2+} release site simulations using 19 four-state models (Eq. 8). Total time: 2 s (*left*) and 50 ms (*arrow*, *right*). For 5 trials the observed mean and variance of N_O are resp. 0.65 ± 0.11 and 6.23 ± 0.82 (mean $\pm$ SD) for a *Score* of 0.50. Parameters as Fig. 3 save $R = 0.5$ μm.

the release site radius is increased from $R = 0.125$ to 0.5 μm.

When specific puffs are plotted in more detail in Figs. 3 and 4 (*arrows*, right panels), we see that the signature of a channel state change is two simultaneous steps, e.g., a $C_2 \rightarrow C_3$ transition implies N_{C_2} decreases and N_{C_3} increases by one. The N_{C_2} and N_{C_3} traces in Fig. 4 show the number of inactivated channels increasing during a puff, suggesting that Ca^{2+}-inactivation is playing a role in the termination of the puff.

Parameters for Figs. 3 and 4 were obtained in a three-step process. First, we searched for a simple measure that agreed with our subjective evaluation of how 'puff-like' responses appeared. We settled on the index of dispersion of the fraction of open channels ($f_O \equiv N_O/N$),

$$Score = \frac{\mathsf{Var}\left[f_O\right]}{\mathsf{E}\left[f_O\right]} = \frac{1}{N}\frac{\mathsf{Var}\left[N_O\right]}{\mathsf{E}\left[N_O\right]}. \tag{29}$$

For binomially distributed N_O, $\mathsf{E}\left[f_O\right] = \pi_O$, and $\mathsf{Var}\left[f_O\right] = \pi_O\left(1-\pi_O\right)/N$. Thus, independently gating channels with small open probability give a (bad) *Score* of $1/N$. The best possible *Score* is 1. Secondly, parameters leading to a high *Score* were identified

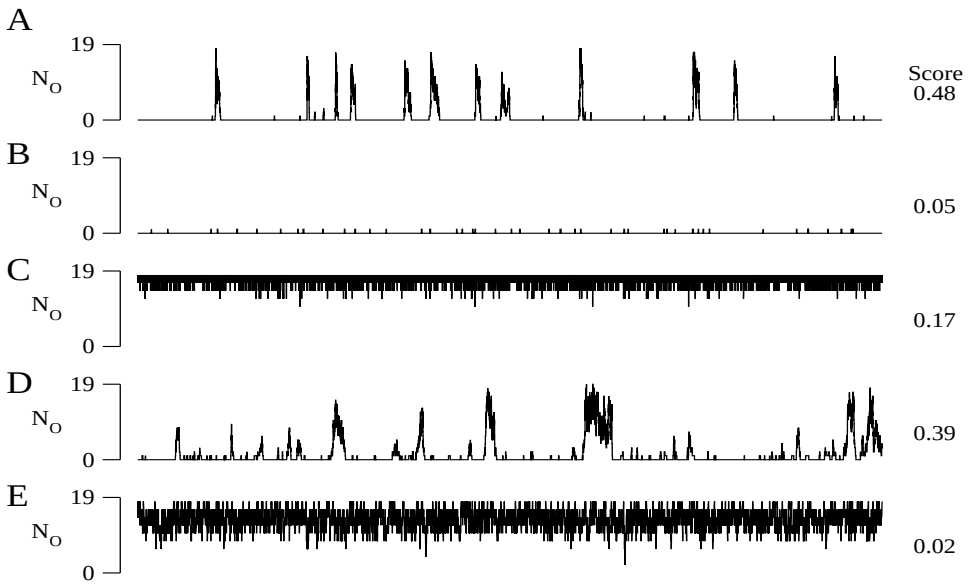

Figure 5: **A**–**C**: Ca^{2+} release sites with 19 four-state channels show Ca^{2+} puffs (**A**, $R = 0.5$ μm) are eliminated when release site density is decreased (**B**, $R = 5$ μm). Turning off Ca^{2+} inactivation (**C**) also eliminates stochastic Ca^{2+} excitability. **D**–**E**: Release site simulations with 19 two-state channels exhibit puffs (**D**, $\eta = 2$) eliminated by decreasing the cooperativity of Ca^{2+} binding (**E**, $\eta = 1$). Total time: 2 s.

through automated random search. Thirdly, channel rate constants were scaled to give reasonable puff duration and inter-puff interval. (Scaling time does not change the *Score* or dynamics of instantaneously-coupled Ca^{2+} release sites.) Parameter studies exploring channel kinetics and cooperativity of Ca^{2+} binding show that stochastic Ca^{2+} excitability, though not uncommon, is not always exhibited by Ca^{2+} release site models (see below). Figures 3 and 4 are representative simulations with a high *Score*.

Figures 5A–C show that the interaction between channels and Ca^{2+}-inactivation is an essential aspect of the puff simulations presented above. The stochastic Ca^{2+} excitability of 19 four-state channels (Fig. 5A, *Score* = 0.48) is eliminated when large release site radius ($c_{ij} \approx 0, i \neq j$) uncouples the channels (Fig. 5B, *Score* = 0.05). Figure 5C shows turning off Ca^{2+}-inactivation ($k_b^{\pm} = k_d^{\pm} = 0$) in the four-state single-channel model can eliminate puffs. Here the number of open channels fluctuates ($14 \leq N_O \leq 19$), but high $\mathsf{E}[f_O]$ leads to low *Score* (0.17). For a summary of these results, see figure 8.

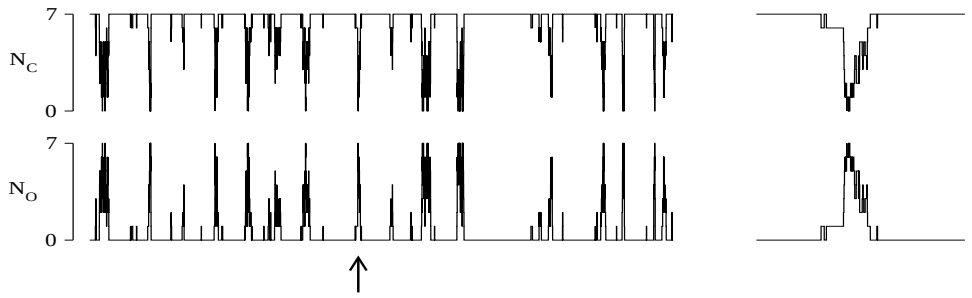

Figure 6: Ca^{2+} release site simulations with 7 two-state models (Eq. 2) show synchronous activation and de-activation (cf. Fig. 4). Total time: 2 s (*left*) and 80 ms (*arrow*, *right*). For 5 trials the observed mean and variance of N_O are resp. 0.52 ± 0.08 and 2.07 ± 0.34 (mean $\pm$ SD) for a *Score* of 0.57. Parameters used: $R = 0.6$ μm, $r_d = 0.05$ μm, $\eta = 2$, $c_\infty = 50$ nM, and $k^\pm$ as Fig. 1A.

4.2 Puff-like behavior does not require Ca^{2+} inactivation

Stochastic excitability exhibited by instantaneously-coupled Ca^{2+} channels can be eliminated by modifying Ca^{2+}-inactivation rates. On the other hand, Figs. 6 and 7 show that automated parameter search using clusters of 7 or 19 two-state channels *without* Ca^{2+} inactivation leads to release sites with high *Score*, as seen in the middle region of Figure 8B (R ≈ 1 μm). Thus, Ca^{2+}-inactivation is not a requirement for the phenomenon of Ca^{2+} puffs. Interestingly, the dynamics of release sites exhibiting puffs in the absence of Ca^{2+} inactivation are irregular and have a broad range of puff amplitudes compared to release sites with Ca^{2+} inactivation (compare Figs. 7 and 4).

Parameters leading to Ca^{2+} puffs are easy to find, even without Ca^{2+} inactivation, and yet most parameter sets do not lead to puffs. When R is increased puffs exhibited by two-state channels (Fig. 5D, *Score* = 0.39) are eliminated and $\mathsf{E}[f_O] \to \pi_O = 0.0074$ (not shown), the steady-state open probability of independently gating two-state channels when $c_\infty = 0.05$ μM (Eq. 5). In Fig. 5E puffs are eliminated by changing the cooperativity of Ca^{2+} binding to the activation site of the two-state channel (**D**: $\eta = 2$; **E**: $\eta = 1$, *Score* = 0.02).

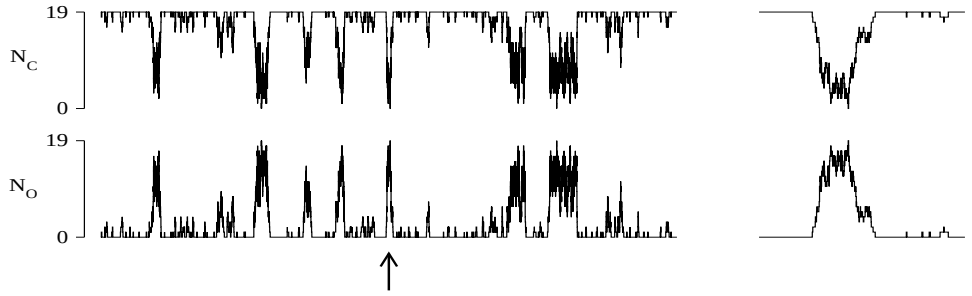

Figure 7: Ca^{2+} release site simulations with 19 two-state models (Eq. 2). Total time: 2 s (*left*) and 80 ms (*arrow*, *right*). For 5 trials the observed mean and variance of N_O are resp. 2.21 ± 0.38 and 18.14 ± 2.65 (mean ± SD) for a *Score* of 0.43. Parameters: $R = 2$ μm and as Fig. 6.

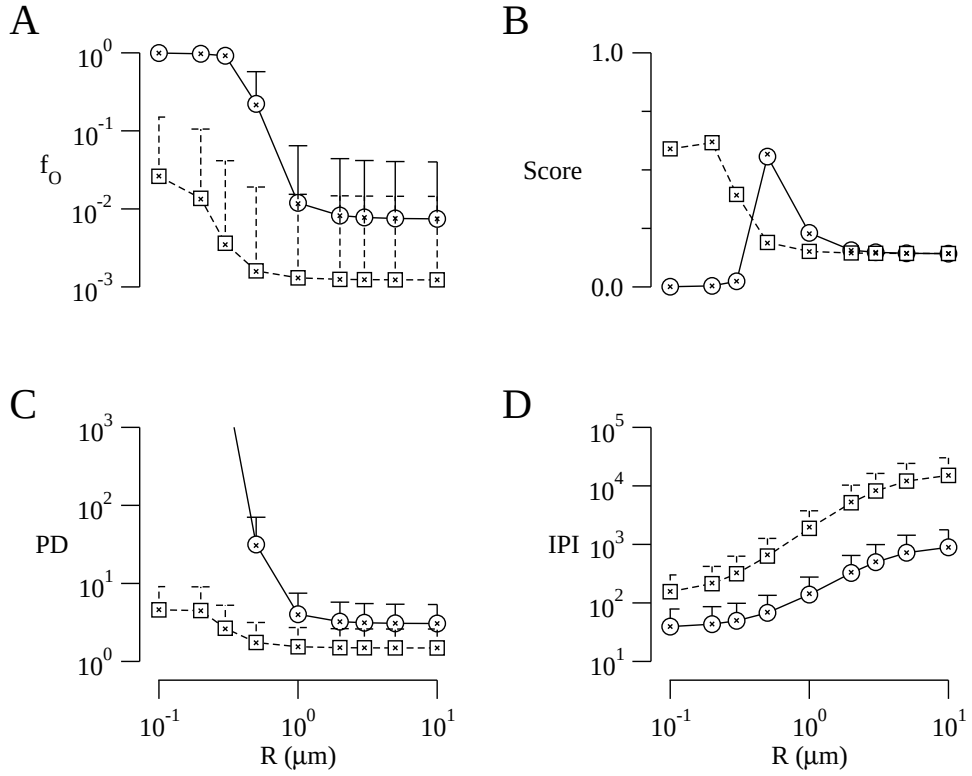

Figure 8: *Open circles* and *error bars* give the expected value and standard deviation of fraction of open channels (**A**), score (**B**), puff duration (**C**), and inter-puff interval (**D**) for a Ca^{2+} release site composed of 7 two-state channels. *Open squares* and *error bars* give results for 7 four-state channels. The x-marks give the result of a simpler calculation that assumes "mean-field" coupling (not discussed here, see [1]. Puff statistics are plotted as a function of the release site radius R.

5 The Fraiman-Ponce Dawson IP_3R model

5.1 Background

Our two- and four-state channel models gave us a good understanding of how coupled channels give rise to puffs in the presence or absence of Ca^{2+}-inactivation. At this point, we were ready to try running simulations using these techniques with more realistic IP_3R channel models. The Fraiman-Ponce Dawson (FPD) IP_3R model incorporates different activation and inactivation mechanisms and reproduces characteristic features of both type-1 IP_3R and type-2 IP_3R single channel gating ([4]). This section explores whether coupled FPD IP_3R models give rise to puffs and how these puffs compare to the dynamics we previously observed using type-1 and type-2 (like two-state) IP_3R channel models.

There is extensive literature discussing the diversity of the three different IP_3R subtypes (types I-III) and how they differ in their affinities for IP_3 and other aspects (see Introduction). Although several models of the IP_3R have been presented in the literature to explain experimental observations differing between one subtype and another there are also discrepancies in experiments involving the same type of IP_3R channel. The discrepancies could be due to numerous factors including different experimental techniques and cell-specific factors such as differing expression levels.

It has been proposed that the concentration of Ca^{2+} residing inside the ER or on the trans side of the chambers used in planar lipid bilayer experiments, may influence IP_3R gating. Although the existence of a luminal Ca^{2+} binding site has long been proposed, the Fraiman–Ponce Dawson is the first IP_3R model to include a luminal Ca^{2+} binding site.

As I was working with this model, I first tried to recreate a few of the paper's graphs, where the authors display the effect of changing concentrations on the channel open probability using a single FPD IP_3R channel. I used the methods discussed in Sec. 3.4, and the list of parameters that they published. However, after numerous simulations, I discovered that none exactly matched the figures found in their paper. I wondered about what could be causing the discrepancies between my own simulations of their model and their published results. After thinking for a while, one possibility that I arrived at was

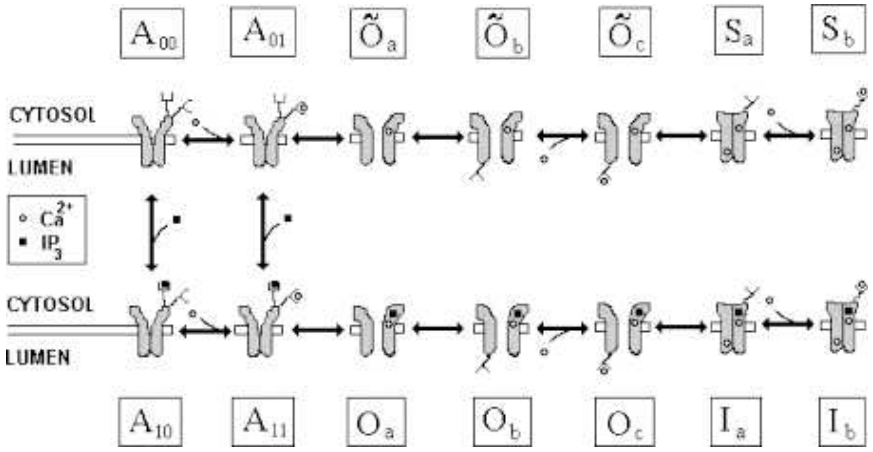

Figure 9: The Fraiman-Ponce Dawson IP_3R model. It consists of 14 different states, and is affected by three different concentrations: $[IP_3R]$, $[Ca^{2+}]_\infty$, and $[Ca^{2+}]_{lum}$. [4].

that perhaps the parameters I was using were different from those the authors used to create their graphs, even though I used the values given in the paper. I contacted the authors, and surely enough, the parameter values that were published were different from those they had used to create their graphs. The authors published an erratum to their paper in response to my query, and with the newly revised parameter values, I was easily able to reproduce similar graphs. With a set of correct parameter values, I ran simulations on a single channel to see the effects of changing Ca^{2+}, IP_3, and $Ca^{2+}{}_{lum}$ concentrations on P_o^{eq}. More recently I have coupled a few of these FPD channels together (using the method presented above) to see if the FPD model exhibited Ca^{2+} puffs.

5.2 Open probability for a single FPD IP_3R channel

The FPD channel model consists of fourteen different states, with three different molecular concentrations affecting rate constants: the $[IP_3]$ influences the channel to switch to the lower branch of the FPD model, cytosolic $[Ca^{2+}]$ binds to the channel to activate it, and the $[Ca^{2+}]_{lum}$ binds to the channel after it is open to inactivate it. Figure 9 shows a schematic picture of the FPD model.

The rate constants used follow [4]. They favor activation in the lower branch, whereas in the upper branch the model is found most likely in the closed and refractory states. Furthermore, in the lower branch of the model, parameters strongly favor an active (open)

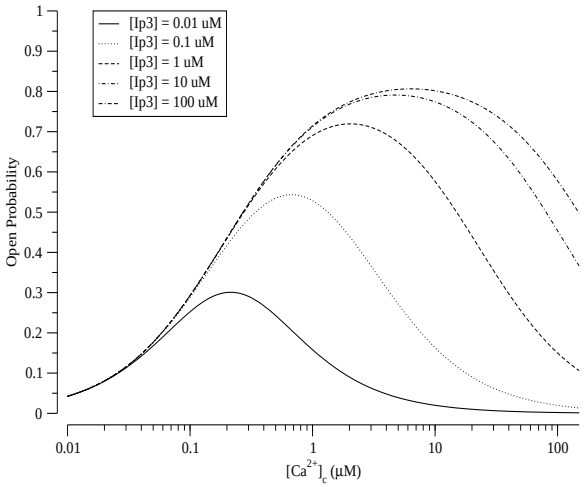

Figure 10: Open probability curves for different values of $[IP_3]$ for the FPD model. Increasing the $[IP_3]$ causes the model to switch to its lower branch, thus increasing the P_o^{eq}, and changing the behavior of the model from a type-I IP_3R to a type-II IP_3R, by shifting the curve upward and widening it.

state, thus making it less likely for the channel transitions to an inactive (closed) state once it reaches state O_a.

This model is more complex than the minimal 2-state and 4-state IP_3R channel models presented above. For example, it includes both luminal regulation and IP_3-potentiation. The model's P_o^{eq} depends on both $[Ca^{2+}]$ and $[IP_3]$ (Fig 10). An important result to note about this graph is that for low $[IP_3]$, the behavior of the FPD IP_3R model is similar to a type-I IP_3R: it has a bell–shape where increasing $[Ca^{2+}]$ first causes activation in the channel and subsequently inactivation. For higher values of the $[IP_3]$, the behavior of the model starts to resemble the type-II IP_3R: increasing $[Ca^{2+}]$ activates the channel but does not fully inactivate it. That is, as we increase $[IP_3]$, it switches the channel into the lower branch, with parameter values that favor activation of the channel, hence causing it to behave more like the type-II IP_3R.

The FPD IP_3R model also incorporates $[Ca^{2+}]_{lum}$ as part of its inactivation mechanism. Once in an open state, a luminal Ca^{2+} ion can bind to the channel to cause it to inactivate, as seen in the right portion of Figure 9. Figure 11 shows that increasing $[Ca^{2+}]_{lum}$ causes the channel to inactivate more rapidly. Again we note that for a small

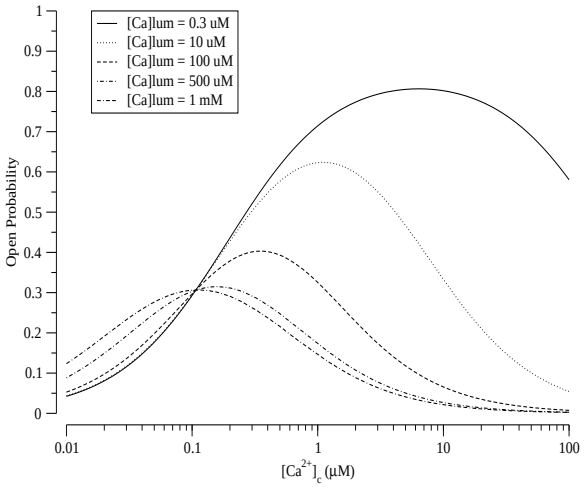

Figure 11: Open probability as a function of $[Ca^{2+}]_{lum}$ for the Fraiman model. With a high $[Ca^{2+}]_{lum}$, the P_o^{eq} curve has a bell shape, and is similar to a type-I IP_3R channel. Decreasing the $[Ca^{2+}]_{lum}$ increases the P_o^{eq}, thus causing the channel to exhibit type-II IP_3R behavior.

$[Ca^{2+}]_{lum}$, the channel behaves similar to a type-II IP_3R channel, with an increasing P_o^{eq} as $[Ca^{2+}]$ increases. For a higher $[Ca^{2+}]_{lum}$, the P_o^{eq} curve shifts downward and becomes more bell–shaped, reminiscent of a type-I IP_3R channel. In this case, the $[Ca^{2+}]_{lum}$ acts as a mechanism for the type-I IP_3R, so decreasing $[Ca^{2+}]_{lum}$ has a similar effect to removing inactivation from the model.

6 Ca^{2+} puffs and the Fraiman-Ponce Dawson Model

Figure 12 shows simulations of coupled FPD IP_3R channels using the expanded generator matrix approach detailed above. Nineteen channels arranged in a hexagonal lattice are allowed to gate for a period of time and we plot the number of open channels as a function of time. Figure 12A shows simulations run with $[Ca^{2+}]_\infty = 0.1$ μM, a physiologically realistic value. The simulation shows no signs of robust puffs and the cluster is rarely completely closed. This may be due to the model exhibiting a tendency to remain in an activated state once it has reached state O_a. Figure 12B shows the same results, except the background calcium has been reduced to $[Ca^{2+}]_\infty = 0.01$ μM (less realistic), in hopes

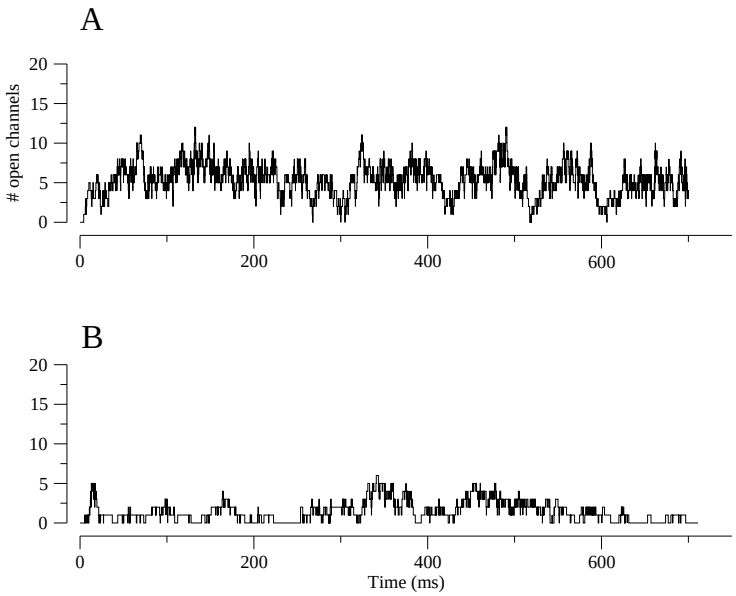

Figure 12: Simulation of 19-coupled FPD IP_3R channels. Both plots show number of open channels as a function of time. Parameter values are $R = 10\mu$m, $[Ca^{2+}]_{lum} = 30$ μM, and $[IP_3] = 0.01$ μM. **A**: $[Ca^{2+}]_\infty = 0.1$ μM, observed open probability was $P_o^{eq} = 0.285$ and $Score = 0.041$. **B**: Parameter values same as in **A**, except $[Ca^{2+}]_\infty = 0.01$ μM. Here $P_o^{eq} = 0.076$ and $Score = 0.061$.

of being able to come up with more of a puffing behavior. Although the channels for the new $[Ca^{2+}]_\infty$ became less active, there was still no signs of clear Ca^{2+} puffs.

We then tried to vary the radius R of the release site to see if there would be a range where the FPD IP_3R model could exhibit puff behavior. Figure 13 shows the N_O (t) for simulations of a range of different radii R. Starting with the smallest value (Fig 13A), we find that in a release site composed of FPD IP_3Rs a few channels are always open. Figure 13C is the closest to show any resemblance of puffs ($R = 5$ μm). For a radius too large, channels no longer interact with each other and become uncoupled (Figure 13D).

Figure 14 shows the fraction of open channels and *Score* for a simulation using parameters from Figure 13C. Figure 14A suggests that the FPD model behaves similar to a type-I IP_3R channel. That is, the open probability starts at its highest value for a small release site radius R and decreases as the radius increases (cf. Figure 8A). The *Score* shown in Figure 14B is low at both extremes—for a small radius and for a large radius—but in the middle the score increases slightly . When Figure 14B is compared to Figure 8B, we see that the FPD model behaves like a type-II IP_3R.

Although we did not observe robust puffs, the simulations using the FPD IP_3R show that this model behaves like a type-I or a type-II IP_3R subunit depending on agonist concentration (Figs 10 and 11). By either increasing $[IP_3]$ or decreasing $[Ca^{2+}]_{lum}$, the model responds similar to a type-II IP_3R, decreasing $[IP_3R]$ or increasing $[Ca^{2+}]_{lum}$ the model responds like a type-I IP_3R.

7 The Bezprozvanny-Ehrlich IP_3R model

The IP_3R model from I. Bezprozvanny and B. Ehrlich [26] has four states, reminiscent of the simple four-state channel model discussed above, and includes three $[Ca^{2+}]$-dependent transitions, one of which is mediated by domain Ca^{2+}. Bezprozvanny and Ehrlich's study of single channel kinetics of IP_3Rs from canine cerebellum showed that conduction properties of these IP_3R Ca^{2+}-channels are similar to that a different family of intracellular Ca^{2+} channels known as ryanodine receptors. Bezprozvanny and Ehrlich estimated the size of the Ca^{2+} current through open IP_3Rs to be approximately 0.5 pA.

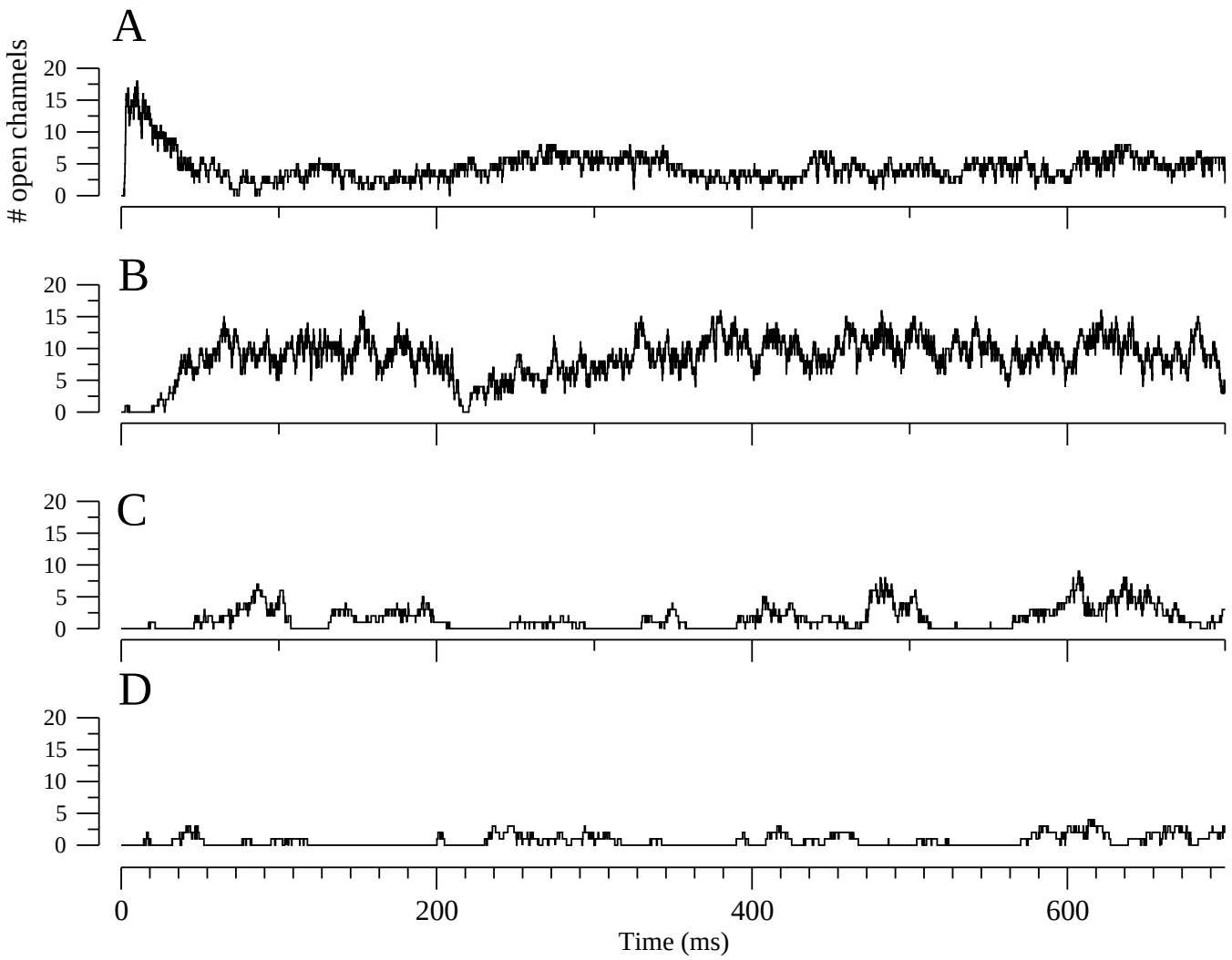

Figure 13: Simulation of 19-coupled FPD IP_3R channel models. Parameter values are the same as Fig 12B ($[Ca^{2+}]_\infty = 0.01$ μM, $[Ca^{2+}]_{lum} = 30$ μM), except the radius R of the release site is varied. **A**: $R = 0.1$ μM, $Score = 0.05785$. **B**: $R = 3$ μm, $Score = 0.06139$. **C**: $R = 5$ μm, $Score = 0.10304$. **D**: $R = 50$ μm, $Score = 0.06309$.

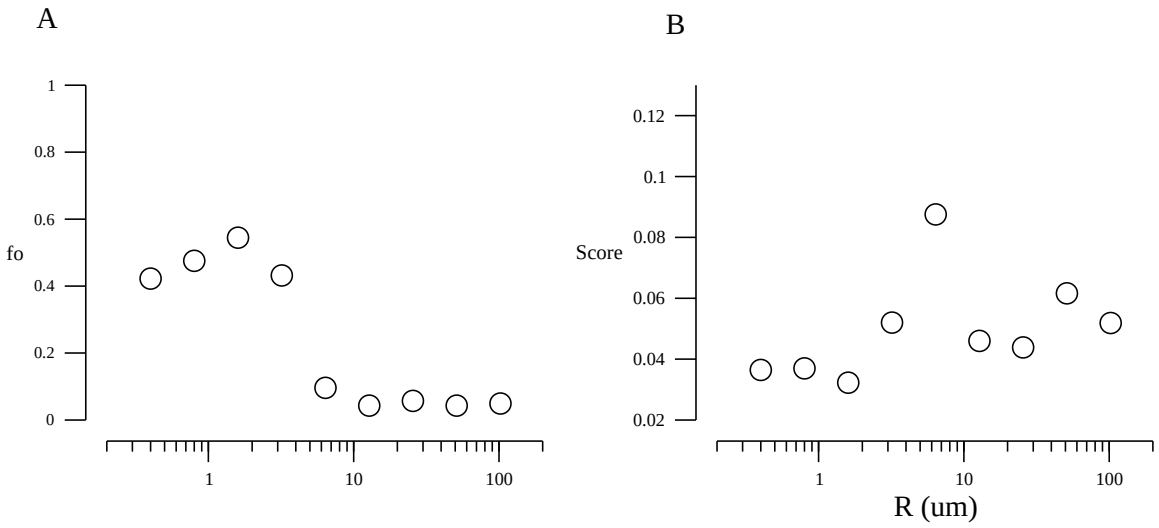

Figure 14: *Open circles* give the value of fraction of open channels (**A**) and score (**B**) for a range of release site radii R. The behavior on the left graph is reminiscent of a type-I IP_3R channel, while the behavior on the right is reminiscent of a type-II IP_3R channel.

7.1 Transition-state diagram of the B-E IP_3R model

The Markov chain model that the authors developed based on their single channel recordings includes a Ca^{2+}-mediated transition that switches it from a closed (C_1) to an activated state (C_2). From there, the channel may open (O) in a $[Ca^{2+}]$-independent manner or another Ca^{2+} ion may bind to the channel moving it into an inactivated, i.e., refractory state (C_3). The transition-state diagram presented in [26] is

$$\begin{array}{ccccc} & & O & & \\ & & \alpha \uparrow\downarrow \beta & & \\ & k_4 c_\infty & & k_3 c_\infty & \\ C_1 & \rightleftharpoons & C_2 & \rightleftharpoons & C_3 \\ & k_5 & & k_2 & \end{array} \qquad \begin{array}{ccc} & k_1(c_\infty + c_d) & \\ O & \rightleftharpoons & C_3 \\ & \gamma & \end{array} \tag{30}$$

where α, β, γ, k_2 and k_5 are unimolecular rate constants, and k_1, k_3, and k_4 are bimolecular rate constants. Note that the transition from the open (O) to the inactivated (C_3) is domain Ca^{2+}-mediated and has been included in Eq. 30 in a manner consistent with the general form of the generator matrix for single channel models presented above (Eq. 1

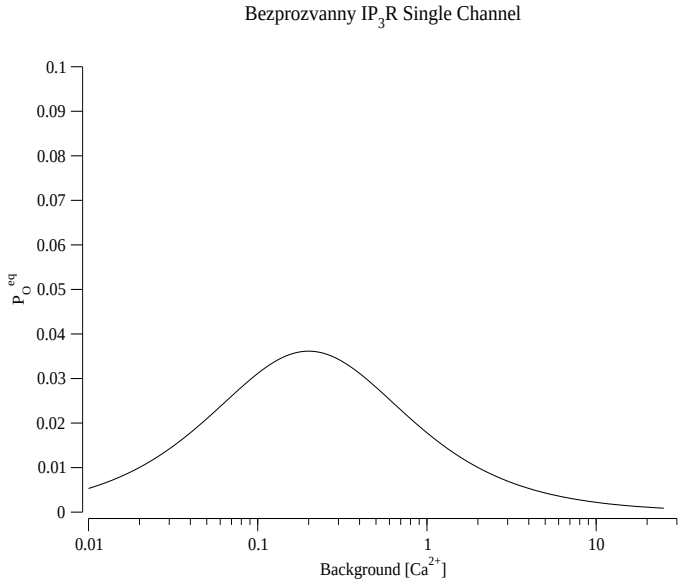

Figure 15: The steady-state open probability for a single B-E IP_3R model [26] is similar to that of the type-I IP_3R channel model presented in Section 3.2. Parameters in s^{-1}: $\alpha = 224$, $\beta = 25.2$, $k_2 = 0.8$, $k_5 = 4$, and γ is chosen to satisfy the thermodynamic constraint ($\gamma = \alpha k_1 k_2 / \beta k_3$). Parameters in μM^{-1} s^{-1}: $k_1 = 57.2$, $k_3 = 4$, and $k_4 = 20$. The cooperativity of Ca^{2+} binding is $\eta = 1$.

and 6). The rate constants used follow [26] (see legend to Figure 15).

7.2 Simulations of coupled B-E IP_3Rs

Figure 15 shows that the P_o^{eq} of the single channel model given by Eq. 30 is a bell-shaped curve, similar to the behavior of the equilibrium open probability of the type-I IP_3R channel discussed in Section 3.2. In order to determine if the B-E IP_3R model could generate Ca^{2+} puffs, I coupled seven of these channel models together, using the instantaneous-coupling paradigm presented in Section 3.7. The background $[Ca^{2+}]$ was set at 0.05 μM and the radius of the release site was varied over a range from 0.05 μm to 1.5 μm. Unfortunately, no robust puffs were observed when using the published parameters, although I did find that the activated state tends to have more activity than the other states. Figure 16 shows a representative simulation of seven B-E IP_3R channel models with a (low) score of 0.1417. Because the IP_3R's spend so much time in

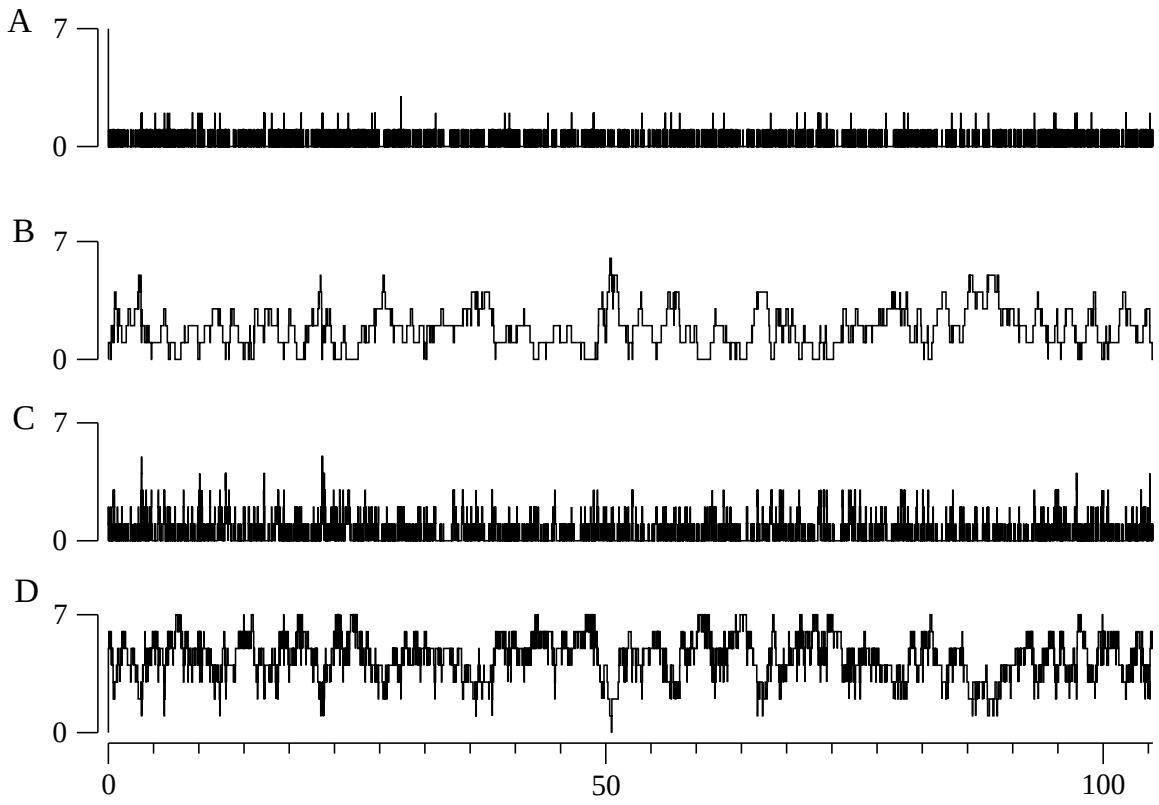

Figure 16: Simulation of 7 B-E IP_3R channel models. From top to bottom, plots show states closed (C_1), activated (C_2), open (O), and refractory (C_3). Rate constants as in Fig. 15, with R = 0.5 μm, $c_\infty = 0.05$ μM. Simulation was run for 100 ms. The *Score* is 0.1417. Behavior is reminiscent of type-I IP_3R channels.

the inactivated state, I decreased the source amplitude (σ) that determines the $[Ca^{2+}]$ increase one channel causes its neighbors to experience. As I expected, lowering σ by a factor of 100 caused the channels to spend much less time in the refractory state (C_3) and more time in the activated state (C_2). However, there was still no sign of robust puffs.

It is interesting that this four-state model and the four-state model of Section 3.2 lead to dramatically different collective behavior when used in model Ca^{2+} release sites. This might not be expected because both models have similar bell-shaped equilibrium open probability curves as a function of background $[Ca^{2+}]$. However, one crucial difference between the simulations presented here and in Section 3.7 is the cooperativity of Ca^{2+} binding in these two IP_3R models. The inability of the B-E IP_3R model to exhibit puffs

may be due to the fact that the cooperativity of Ca^{2+} binding is $\eta = 1$, while in Section 3.2 $\eta = 2$. Also, in Section 3.2 a large number of parameter sets were explored, only some of which led to puffs. If similar parameter studies were performed for the B-E IP_3R model, it is possible that some might lead to puffs.

8 Effect of spatial arrangement of Ca^{2+} channels on the puff Score

The simulations of coupled channels above have consistently used a hexagonal lattice (or "honeycomb") arrangement, and, consequently, channel location is the same in every simulation. However, the location of each channel in Ca^{2+}release sites can be chosen in other ways. This section explores the effect of different spatial arrangements on the puff *Score* of coupled Ca^{2+}-regulated Ca^{2+} channels.

Figure 17 shows two different arrangements for seven IP_3R channels. In both cases, the radius of the release site is $R = 0.5$ μm. Because of the fixed spatial location in the honeycomb arrangement, the parameters of the coupling matrix $C = (c_{ij})$ will always stay the same (Section 3.5). The right panel of Figure 17 shows channel positions drawn from a *uniform distribution* on a disk of radius R = 0.5 μm. Here the position of the channels and the strength of the coupling matrix changes for each simulation. Whereas the *Score* for simulations using a honeycomb arrangement are nearly constant for sufficiently long simulations, the *Score* for simulations using uniformly distributed channels will exhibit a range of values consistent with the random distribution of channel positions.

Figure 18 shows the different ranges of the Ca^{2+} puff *Score* and the fraction of open channels (f_o) when running simulations for seven two-state (panels A and B) IP_3R channels or seven four-state (panels C and D) IP_3R channels with positions chosen from a uniform distribution. For both the fraction of open channels and the *Score*, the two-state channel model exhibits a wider range of values than the four-state channel model, for example, from 0 to almost 0.8 in Fig 17A. In contrast, Fig 17C shows similar results for the four-state channel model; the range is from 0 to 0.04, narrower than Fig 17A. We in-

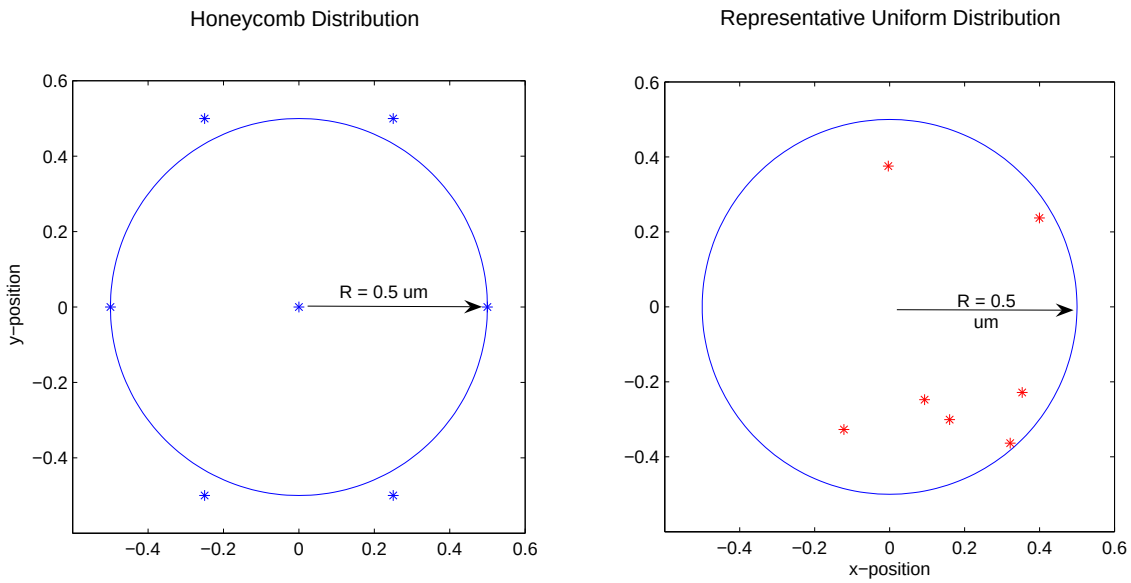

Figure 17: Different spatial arrangements for 7 channels. Left: a hexagonal lattice (honeycomb) arrangement as discussed in Section 3.5. Right: a representative plot of channel positions selected from a uniform distribution of radius R.

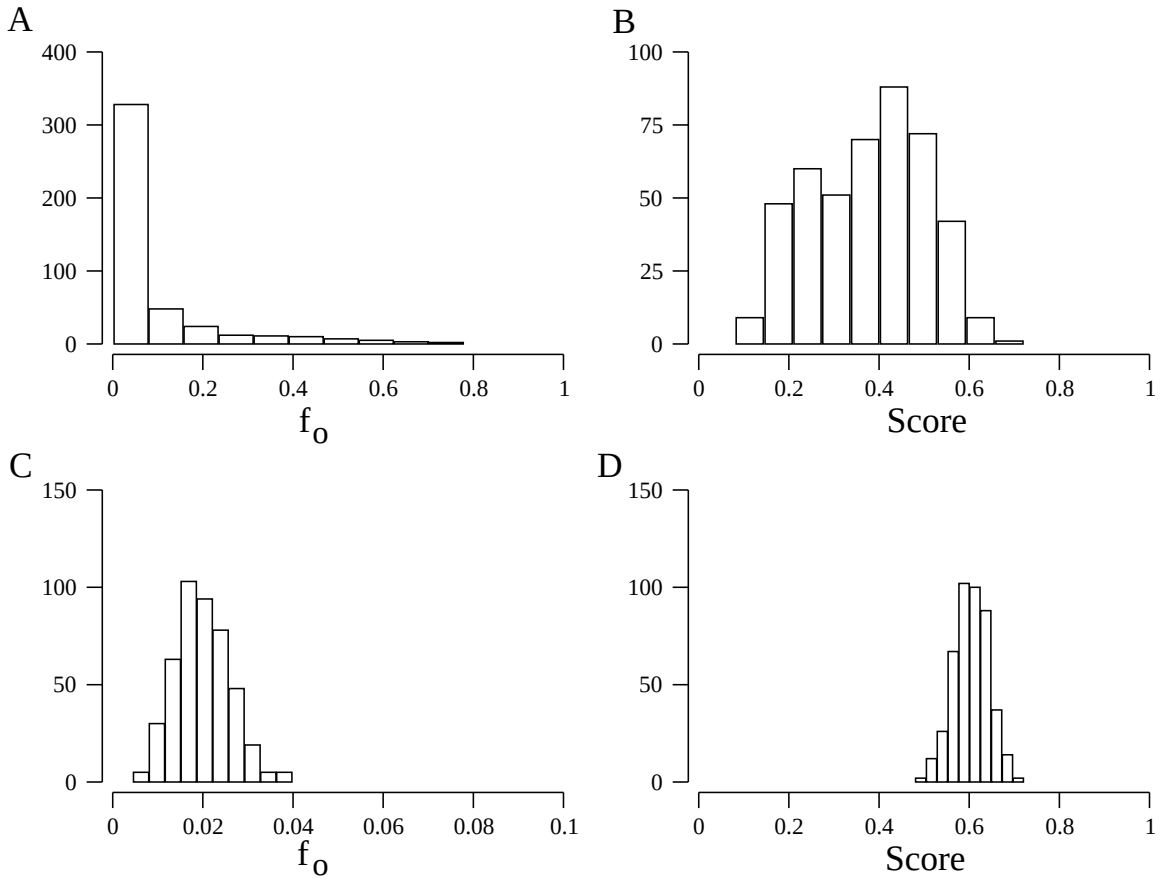

Figure 18: Distribution for fraction of open channels (f_o) and puff Score when channel positions are chosen from a uniform distribution on a disk of radius R. A, C: seven two-state IP_3R channel similar to Fig. 3. B, D: seven four-state IP_3R channels, similar to Fig. 6.

terpret these results as a demonstration that release sites composed of four-state channel models are less sensitive to the exact position of the channels than the two-state model, presumably because of the presence of Ca^{2+} inactivation in the former case. Figure 18C and D show the range *Scores* for simulations using two-state channels and four-state channels, respectively. The range is again much greater for two-state channels, signifying that the precise location of the channels within the cluster influences puff dynamics to a larger degree when Ca^{2+} inactivation is not present in the single channel model. Figure 19 shows representative channel arrangements leading to particularly low and high *Scores*.

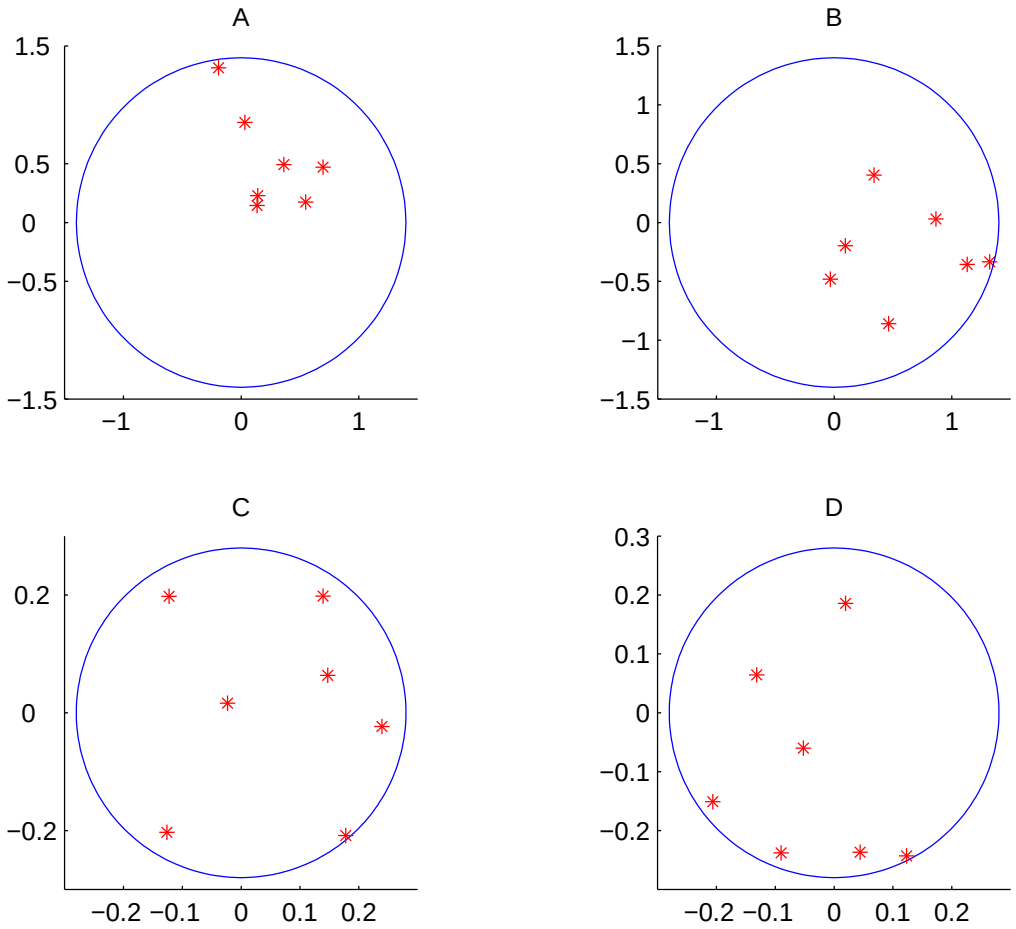

Figure 19: Representative channel locations leading to particularly low (*left column*) and high (*right column*) *Score*. Top: simulations using two-state IP_3R channels. Bottom: simulations using four-state IP_3R channels.

Acknowledgments

I would like to thank Dr. Smith for advising this research project, including helpful discussions, editing, and finalization of figures 1-9. I would also like to acknowledge Dr. Roy Mathias's contribution to the development of memory-efficient methods used in the *SAN* descriptor approach and Vivian Zhang for occasional assistance.

References

[1] R. M. V. Nguyen and G. Smith, Bulletin of Mathematical Biology **67**, 393 (2005).

[2] B. Plateau and W. Stewart, Stochastic automata networks, in *Computational Probability*, edited by W. Grassmann, pages 113–151, Kluwer Academic Publishers, Boston, 2000.

[3] W. Stewart, *Introduction to the Numerical Solution of Markov Chains*, Princeton University Press, 1994.

[4] D. Fraiman and S. Ponce-Dawson, Cell Calcium **35**, 403 (2003).

[5] M. Berridge, Nature **361**, 315 (1993).

[6] M. Berridge, J Physiol (London) **499**, 291 (1997).

[7] M. Berridge, Neuron **21**, 13 (1998).

[8] N. Allbritton, T. Meyer, and L. Stryer, Science **258**, 1812 (1992).

[9] X. Sun, N. Callamaras, J. Marchant, and I. Parker, J Physiol **509**, 67 (1998).

[10] Y. Yao, J. Choi, and I. Parker, J Physiol **482**, 533 (1995).

[11] I. Parker, J. Choi, and Y. Yao, Cell Calcium **20**, 105 (1996).

[12] H. Cheng, W. Lederer, and M. Cannell, Science **262**, 740 (1993).

[13] H. Cheng, M. Lederer, W. Lederer, and M. Cannell, Am J Physiol **270**, C148 (1993).

[14] E. Niggli, Annu Rev Physiol **61**, 311 (1999).

[15] D. Bers, *Excitation-Contraction Coupling and Cardiac Contractile Force*, Kluwer Academic Publishers, second edition, 1992.

[16] M. Cannell, H. Cheng, and W. Lederer, Science **268**, 1045 (1995).

[17] S. Joseph, Cell Signal **8**, 1 (1996).

[18] A. Maranto, J Biol Chem **269**, 1222 (1994).

[19] R. Hagar, A. Burgstahler, M. Nathanson, and B. Ehrlich, Nature **396**, 81 (1998).

[20] J. Ramos-Franco, M. Fill, and G. Mignery, Biophys J **75**, 834 (1998).

[21] M. Bootman and P. Lipp, Curr Biol **9**, R876 (1999).

[22] D. Mak et al., J Gen Physiol **115**, 241 (2000).

[23] E. Kaftan, B. Ehrlich, and J. Watras, J Gen Physiol **110**, 529 (1997).

[24] G. De Young and J. Keizer, Proc Natl Acad Sci USA **89**, 9895 (1992).

[25] A. Atri, J. Amundson, D. Clapham, and J. Sneyd, Biophys J **65**, 1727 (1993).

[26] I. Bezprozvanny and B. Ehrlich, J Gen Physiol **104**, 821 (1994).

[27] Y. Tang, J. Stephenson, and H. Othmer, Biophys J **70**, 246 (1995).

[28] S. Swillens, P. Champeil, L. Combettes, and G. Dupont, Cell Calcium **23**, 291 (1998).

[29] I. Moraru, E. Kaftan, B. Ehrlich, and J. Watras, J Gen Physiol **113**, 837 (1999).

[30] A. LeBeau, D. Yule, G. Groblewski, and J. Sneyd, J Gen Physiol **113**, 851 (1999).

[31] E. Neher, Exp Brain Res **14**, 80 (1986).

[32] F. Sala and A. Hernandez-Cruz, Biophys J **57**, 313 (1990).

[33] J. Wagner and J. Keizer, Biophys J **67**, 447 (1994).

[34] G. Smith, Biophys J **71**, 3064 (1996).

[35] M. Gabso, E. Neher, and M. Spira, Neuron **18**, 473 (1997).

[36] M. Naraghi and E. Neher, J Neurosci **17**, 6961 (1997).

[37] E. Neher, Cell Calcium **24**, 345 (1998).

[38] G. Smith, L. Dai, R. Muira, and A. Sherman, SIAM J Appl Math **61**, 1816 (2001).

[39] J. Marchant and I. Parker, Biochem J **334**, 505 (1998).

[40] S. Dargan and I. Parker, J Physiol **553**, 775 (2003).

[41] D. Colquhoun and A. Hawkes, A Q-matrix cookbook: how to write only one program to calculate the sigle-channel and macroscopic predictions for any kinetic mechanism, in *Single-Channel Recording*, edited by B. Sakmann and E. Neher, pages 589–633, Plenum Press, New York, 1995.

[42] G. Smith, Modeling the stochastic gating of ion channels, in *Computational Cell Biology*, edited by C. Fall, E. Marland, J. Wagner, and J. Tyson, pages 291–325, Springer-Verlag, 2002.

[43] T. Hill, *Free Energy Transduction in Biology: the steady-state kinetic and thermodynamic formalism*, Academic Press, New York, 1977.

[44] G. Smith, An extended DeYoung-Keizer-like IP_3 receptor model that accounts for domain Ca^{2+}-mediated inactivation, in *Recent Research Developments in Biophysical Chemistry, Vol. II*, edited by C. CA and B. A, Research Signpost, 2002.

[45] A. Sherman, J. Keizer, and J. Rinzel, Biophys J **58**, 985 (1990).

[46] W.-H. Steeb, *Matrix calculus and Kronecker product with applications and C++ programs*, World Scientific, 1997.

[47] A. Langville and W. Stewart, J Comput Appl Math (2003), Accepted.

[48] B. Plateau and K. Atif, IEEE Trans. Software Eng. **17**, 1093 (1991).

[49] R. Horn and C. Johnson, *Topics in Matrix Analysis*, Cambridge University Press, 1991.